

Mechanical properties and rolling-sliding wear performance of dual phase austempered ductile iron as potential metro wheel material



Hua Zhang, Yanxin Wu, Qiuju Li*, Xin Hong

State Key Laboratory of Advanced Special Steel & Shanghai Key Laboratory of Advanced Ferrometallurgy & School of Materials Science and Engineering, Shanghai University, Shanghai 200072, China

ARTICLE INFO

Keywords:

Dual phase austempered ductile iron
Intercritical austempering
Mechanical properties
Wear
Delamination

ABSTRACT

Dual phase austempered ductile iron (dual phase ADI) was produced through intercritical austempering with various partially austenitizing temperatures. Partial austenitization within the intercritical interval has a profound influence on the amount and morphology of microstructure in dual phase ADI. The influence of partially austenitizing temperatures on the mechanical properties and rolling-sliding wear performance of dual phase ADI were also investigated. The results show steady increases in the tensile strength and yield strength with increasing partially austenitizing temperature, while the opposite behavior is observed for elongation. The optimum combination including ultimate tensile strength of 746 MPa, impact toughness of 125 J and elongation of 14% is obtained in the dual phase ADI partially austenitized at 810 °C, which is composed of 20% proeutectoid ferrite and 80% ausferrite constituent. Wear behavior could be understood from the manner the hardened layer fragmented and detached. The main wear mechanism under air cooling condition is delamination due to sub-surface deformation. Wear rate decreases as matrix hardness increases. According to the results of mechanical and wear tests, dual phase ADI partially austenitized at 810 °C demonstrates superior wear performance as well as relatively reasonable mechanical properties, suggesting the potential of this material for application in metro wheels.

1. Introduction

Austempered ductile iron (ADI), combining excellent ratio of strength to weight [1], good fatigue strength [2], excellent wear resistance [3–5], high fracture toughness [6,7] and excellent design flexibility [8], has been used extensively in many structural applications, such as automotive components, gears, earth moving machinery and rail equipment [9–11]. The ADI consists of an ausferrite (AF) matrix microstructure, characterized by the existence of bainite ferrite (BF) and high carbon retained austenite (RA). The heat treatment responsible for the specific microstructure involves complete austenitization followed by austempering at a temperature ranging from 260 °C to 400 °C. During austempering treatment, ductile iron undergoes a two-stage transformation process [12]. The martensite from the stage I reaction and carbide from the stage II reaction are unfavorable for ductility and toughness. Thus, the optimum combination of strength and ductility in ADI is obtained within the time period between the completion of stage I and the onset of stage II, referred as the ‘process window’ [13].

However, the large amount of austenite in conventional ADI usually

results in much work-hardening of materials and will deteriorate the machinability of ADI. Furthermore, absence of proeutectoid ferrite (PF) in conventional ADI limits the ductility of ADI. To overcome the limitations of conventional ADI, a new type of ductile iron, called ‘dual phase ADI’, has become an active focus of research and manufacturing [14–18]. The dual phase ADI consists of different amounts and morphologies of AF constituent (conventional ADI microstructure) and PF constituent, which can be achieved by intercritical austempering [19,20]. The special heat treatment is a process wherein ductile iron is partially austenitized within the intercritical interval (delimited by the upper and lower critical temperatures [21]) where graphite, ferrite and austenite co-exist, followed by an austempering step. It was noted that the position and amplitude of the interval changes with the chemical composition [22]. Additionally, dual phase ADI could provide a wide range of mechanical properties as a function of the relative proportion of PF and AF constituents, thereby replacing ductile iron with other matrices [23]. Therefore, dual phase ADI will be appropriate for new applications in the critical parts, where a combination of high strength and ductility is a pressing requirement.

With regard to research on the optimization of wheel materials,

* Corresponding author.

E-mail address: liqiujuiron@163.com (Q. Li).

<https://doi.org/10.1016/j.wear.2018.04.005>

Received 16 January 2018; Received in revised form 8 April 2018; Accepted 9 April 2018

Available online 10 April 2018

0043-1648/ © 2018 Published by Elsevier B.V.

designers should balance the cost, weight, wear resistance, noise reduction and rolling contact strength [24]. Conventional ADI, with higher damping capacity and lower density, is suitable as an alternative material for railcar wheels [25–27]. Correspondingly, dual phase ADI, which exhibits much greater ductility and machinability than conventional ADI, may be applied to metro wheels, which demand lower rolling contact strength due to the working conditions of lower speed and lighter weight. Considering the application of dual phase ADI as a substitute for steels in the field of metro wheels, it is thus crucial to investigate its wear performance matched with conventional rail steel. The reason is that metro wheel materials are limited in service by adhesive wear and rolling contact fatigue wear, which are the main damage types of wheel/rail [24]. Many wear investigations concerning ductile irons have been conducted previously. Sahin et al. [28] studied the abrasive wear behavior of ADI with dual matrix structures and found that wear resistance increased with increasing AF volume fraction or decreasing austempering time. Bedolla-Jacuinde et al. [3] analyzed the wear resistance under dry sliding conditions of an ADI microalloyed with different amount of boron and concluded that both specific wear rate and friction coefficient increased slightly with the boron content due to the lower hardness obtained through this element. Zhang et al. [27] conducted rolling-sliding wear tests of ADIs with three strength grades matched with conventional rail steel. The results revealed that the increase of subsurface hardness was due to work-hardening and strain-induced transformation of retained austenite to martensite and the main wear mechanism was delamination.

However, no efforts have been so far made to investigate the dry rolling-sliding wear performance of dual phase ADI matched with conventional rail steel, which is an important consideration for designers of metro wheels. Therefore, the purpose of this investigation was to study the influence of intercritical austempering with different partially austenitizing temperatures on the mechanical properties and rolling-sliding wear performance of dual phase ADI. In addition, microstructural evolutions during intercritical austempering were characterized using an optical microscope (OM), X-ray diffraction (XRD), and a scanning electron microscope (SEM). Meanwhile, the fracture surface, wear behavior as well as wear mechanism of dual phase ADI were discussed in detail.

2. Experimental procedure

As-cast alloyed ductile iron with the chemical composition, displayed in Table 1, was prepared by induction melting and cast into 25 mm Y-blocks. As shown in a previous study, the material consisted of pearlite and PF constituents surrounding graphite nodules with 85% nodularity, and had a yield strength of 372 MPa, tensile strength of 676 MPa, and elongation of 8.6%. The preliminary investigation was performed to determine the intercritical interval and study the influence of partially austenitizing temperatures on the fraction of PF constituent. For this purpose, samples of 40 × 25 × 10 mm, machined from the bottom section of Y-blocks, were annealed for 60 min around the calculated intercritical interval, which was estimated to range from 770 °C to 799 °C using empirical equations [29,30]. The samples were then quenched in water at room temperature. The fraction of PF constituent was determined with the assistance of Image-Pro Plus software.

Based on the results of preliminary investigation, heat treatment cycles employed to produce dual phase ADI consisted of a first step of partial austenitization, in which samples of 155 × 40 × 12.5 mm were

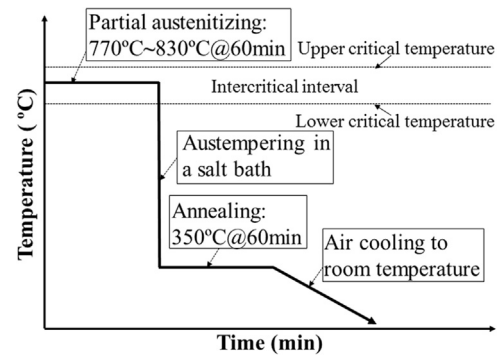


Fig. 1. Heat treatment cycles employed to produce dual phase ADI.

held at temperatures within the actual intercritical interval, followed by an austempering step of 350 °C in a salt bath containing 50% KNO₃ + 50% NaNO₃, as shown in Fig. 1. The austenitizing temperatures employed were 770, 790, 810, and 830 °C, respectively. In all cases, austenitizing and austempering times were both 60 min. The samples were labeled according to matrix structure and partially austenitizing temperature and coded as D770, D790, D810, and D830, respectively. For reference, conventional ADI was also produced through complete austenitization and coded as C900. After the heat treatment above, microstructural characterization, mechanical properties and rolling-sliding wear performance were investigated to evaluate the potential of dual phase ADI as metro wheel material. For this reason, metallographic specimens, tensile specimens (gauge length Φ5 × 30 mm), Charpy impact specimens, and rolling-sliding wear specimens were machined from the heat-treated samples, respectively.

Metallographic specimens were examined by OM (Axio Cam MRC5) and SEM (ZEISS SUPRA 55) after being ground, polished, and etched with 4 vol% Nital. The fraction of PF constituent was evaluated from the results of preliminary investigation. It should be noted that graphite was not taken into consideration when characterizing the fraction of reported constituents. The fraction of RA constituent was determined using the direct comparison method based on the typical intensities of austenitic peak and ferritic peak [31,32]. XRD was carried out using monochromatic copper K α radiation at 40 kV and 40 mA. A Bruker Phaser II diffractometer was used to scan at the 2 θ angle, ranging from 20° to 90° with an angular speed of 2°/min. The profile was then analyzed using Jade 5 software to obtain the peak positions and the integrated intensities for the (111), (200) and (220) planes of FCC and the (110), (200) and (211) planes of BCC. Additionally, the fraction of BF constituent was obtained by subtracting that of RA constituent from that of AF constituent. The carbon content of the austenite was determined by the equation [33]:

$$a_{\gamma} = 3.555 + 0.044C_{\gamma}$$

where a_{γ} is the lattice parameter of austenite (Å) and C_{γ} is the carbon content (wt%). The (111) planes of austenite were used to estimate the lattice parameter.

Tensile tests were conducted following the specifications given by ASTM E8/E8M-2009 [34] using a universal testing machine (20-t SANS) with a cross-head speed of 1 mm/min at room temperature. The tensile properties, including ultimate tensile strength (UTS), yield strength (YS) and elongation (E_{ℓ}), were calculated as the averages of three tests. After the test, the fracture surface was analyzed by SEM to characterize the fracture mechanisms. Furthermore, Impact toughness was measured based on the average of three unnotched Charpy impact tests. In addition, Vickers hardness of matrix structure was examined with an MH-5 tester applying a load of 490 mN (HV_{0.05}). Average values were obtained based on 10 measurements.

Based on Chinese standard GB/T 12444.1-1990 [35], dry rolling-sliding wear tests were conducted on the disc-on-disc configuration,

Table 1

Chemical composition of as-cast ductile iron (wt%).

Element	C	Si	Mn	P	S	Cu	Ni	Mg
Composition (%)	3.62	2.67	0.13	0.05	0.01	0.62	0.63	0.04

*The carbon equivalent of the alloyed ductile iron was 4.51.

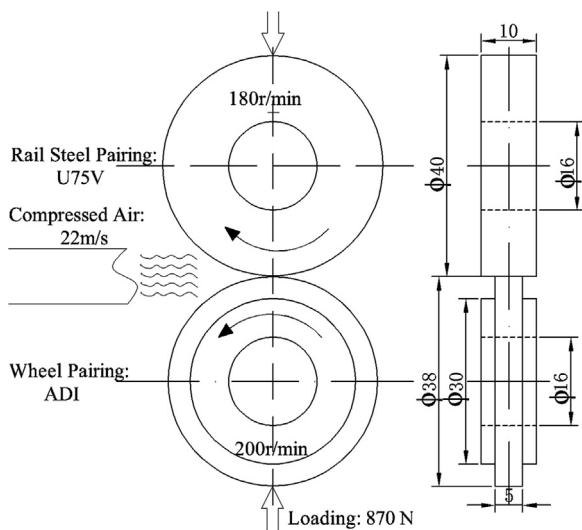


Fig. 2. Schematic diagram of dry rolling-sliding wear tests.

which could ensure a line contact between two wear pairings. Fig. 2 presents a schematic diagram of dry rolling-sliding wear tests. The upper pairing with a surface roughness of 0.8 was made of rail steel (U75V), which was machined from the top surface of railhead and had a hardness of 350 HV. Meanwhile, the lower pairings were machined from the heat-treated samples with a same surface roughness of 0.8. The rotational speed of U75V pairing was 180 r/min, and that of ADI pairing, 200 r/min. Correspondingly, this led to a slip ratio of 5.4%. The contact width between two pairings was 5 mm. To simulate the wear behavior in actual metro working conditions, all the tests were conducted under a high contact load of 870 N. According to Johnson's equations [36], the maximum Hertz's reference pressure was about 800 MPa. Considering air cooling induced by strong wind in actual conditions, the contact region between two pairings was continuously cooled by a blast of dry compressed air with a speed of 22 m/s. During the tests, each pairing was subjected to a running-in for the first 20,000 rolling cycles to remove the machining layer. Upon completion of the running-in, the pairings were remounted in the same locations to conduct subsequent 80,000 cycles. The friction coefficient of the latter stage was recorded during the test. The weight loss of worn pairings during the latter stage was determined using an electronic balance with an accuracy of 1 mg. Average wear rate as a function of rolling distance was calculated as the average weight loss of two tests. After the tests, subsurface of worn ADI pairings was characterized through microstructural observation and Vickers hardness measurements on the cross section of worn pairings. In addition, worn surface was characterized by SEM and XRD to analyze the wear behavior and wear mechanism.

3. Results and discussion

3.1. Determination of intercritical interval

The intercritical interval was determined according to the procedure described in the 'Experimental Procedure' section. Fig. 3 illustrates microstructures of ductile irons obtained after heating at different partially austenitizing temperatures and water quenching. They generally consist of graphite (black region), ferrite (white region) and martensite (gray region). It should be noted that martensite was fully formed at the temperature of 850 °C, indicating that a holding time of 60 min is enough to reach equilibrium. On heating of the sample within the intercritical interval, ferrite and/or pearlite constituents converted to austenite, starting at the eutectic cell boundaries, which was thought to transform into martensite during quenching process. In addition, the fraction of remaining ferrite around graphite nodules depends on

partially austenitizing temperature, which corresponds to the PF constituent presented in dual phase ADI.

Fig. 4 shows measured fractions of ferrite and martensite as a function of partially austenitizing temperature. It can be seen that the amount of ferrite decreases, whereas that of martensite increases, as the temperature increases. The lower critical temperature is defined as 750 °C due to observation of the beginning of transformation from ferrite to austenite. Simultaneously, the upper critical temperature is established at 850 °C, taking the presence of 99% martensite into account. Accordingly, the actual intercritical interval ranges from 750 °C to 850 °C, which shows an underestimation of the upper critical temperature by the empirical equations [29,30].

3.2. Microstructural characterization

Fig. 5 shows microstructural morphologies of ADIs. As shown, matrix structure of all dual phase ADIs generally consists of different proportions of AF and PF constituents, depending on partially austenitizing temperature. The morphology also varies with the temperature. The restriction of AF constituent to the eutectic cell boundaries in an isolated or continuous network depends on its proportion. For example, D770, with the lowest fraction of AF constituent, shows that ferrite around graphite nodules is barely surrounded by AF constituent, as shown in Fig. 5(a). However, C900 exhibits nearly wholly AF constituent, as shown in Fig. 5(e). Furthermore, detailed microstructural characterizations of ADIs are listed in Table 2. It was found that with a reduction of partially austenitizing temperature, the fraction of PF constituent increases, while that of AF constituent decreases, as also plotted in Fig. 6, which yields the same trend reported previously [18–20,28].

During the austempering step, BF constituent with a feathery-like shape initially formed to replace the unstable austenite, which is difficult to distinguished from PF constituent due to epitaxial growth of BF constituent from the existing ferrite [37], and RA constituent resided simultaneously between the BF plates. This formation occurs because excess carbon is redistributed into the surrounding retained austenite, which becomes stabilized without the risk of martensite formation when cooled to room temperature [38,39]. Additionally, it should be mentioned that no martensite or decomposition carbides exists after the treatment, indicating that the adopted austempering time is suitable.

The XRD patterns obtained from ADIs are shown in Fig. 7. The (111), (200) and (220) planes of FCC, the (110), (200) and (211) planes of BCC, and the (002) plane of graphite were identified, substantiating the microstructure observed in the SEM micrographs. As shown in Fig. 7, increasing partially austenitizing temperature has a significant effect on the integrated intensity for austenite, especially for the increase in the (111) plane, due to the formation of RA constituent.

Furthermore, detailed microstructural characterizations of the AF constituent calculated from the diffraction patterns, such as the carbon content in RA constituent and the fraction of RA and BF constituents, are listed in Table 2. As the fraction of AF constituent increases, the fraction of RA and BF constituents both increase considerably, as also plotted in Fig. 6. It should be mentioned, however, that the fraction of BF constituent drops adversely in C900. The equilibrium carbon content of austenite (C_{γ}^0) is determined by the empirical equation $C_{\gamma}^0 = (T_{\gamma}/420) - 0.17W_{Si} - 0.95$ proposed by Voigt [40], which describes the solubility of carbon in austenite as a function of austenitizing temperature T_{γ} and silicon content W_{Si} for cast iron. Increasing the temperature improves the enrichment of carbon in the austenite, which leads to the fraction of BF constituent dropping and raises the carbon content in RA constituent, as also plotted in Fig. 6. Accordingly, it was concluded that partial austenitization within the intercritical interval has a profound influence on the amount and morphology of microstructure in dual phase ADI.

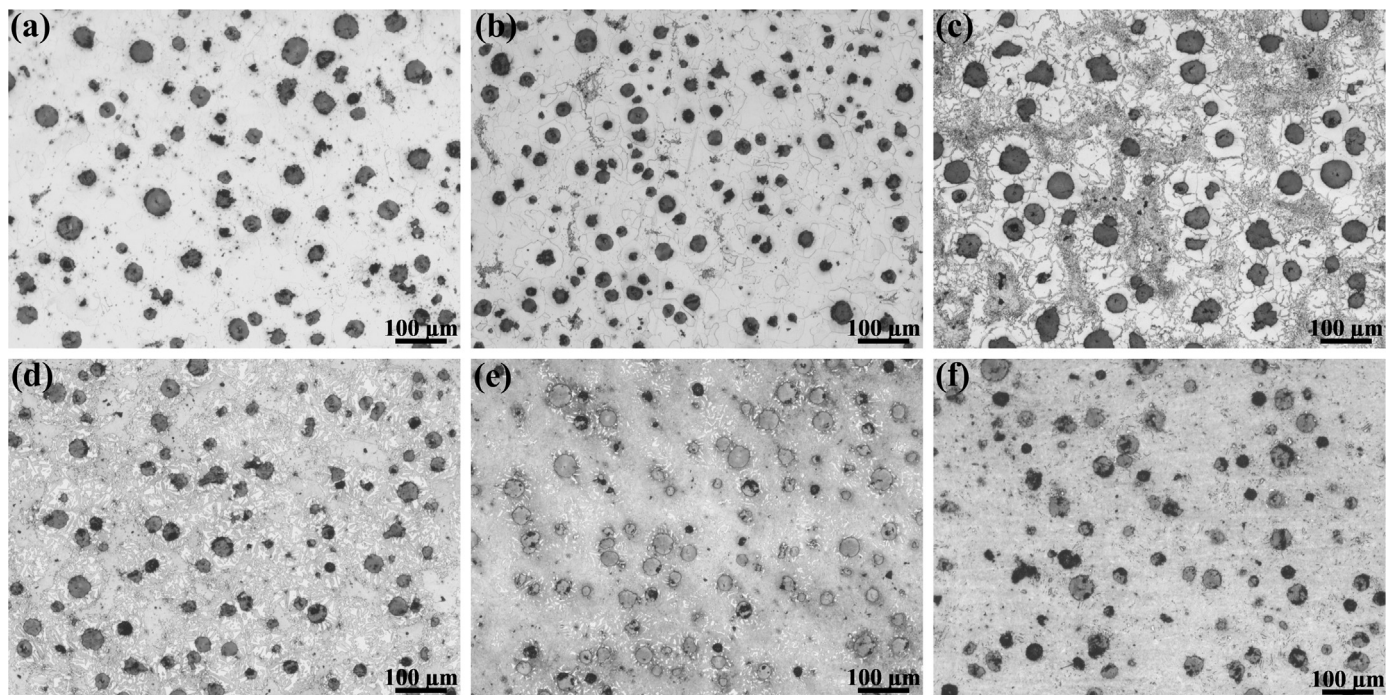


Fig. 3. Microstructure of ductile irons obtained after heated at different partial austenitizing temperatures and water quenched: (a) 750 °C; (b) 770 °C, (c) 790 °C, (d) 810 °C, (e) 830 °C, (f) 850 °C.

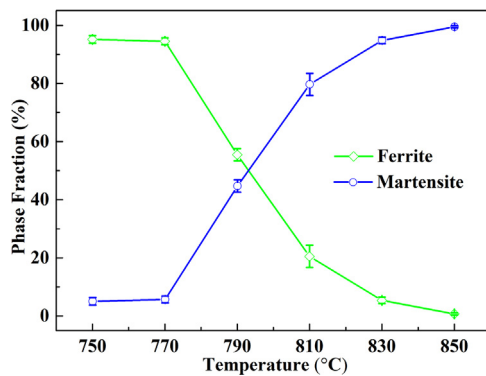


Fig. 4. Measured fraction of ferrite and martensite as a function of partial austenitizing temperature.

3.3. Mechanical properties

Table 3 summarizes mechanical properties of ADIs. The results reveal that dual phase ADI can offer a wide range of mechanical properties depending on its matrix structure, which shows an improvement in the combination of UTS and E_f with respect to that of the as-cast ductile iron mentioned in the Section 2. The improvement is attributed to the location of AF constituent in the last-to-freeze regions, which are the weakest areas in the matrix, where it acts as a reinforcing phase [41]. As expected, a steady increase is noticed in the UTS and YS with increasing partially austenitizing temperature, while the opposite behavior is observed in the E_f yielding lower values, which is attributed to the reduction of PF constituent and the increase of AF constituent in matrix structure, as plotted in Fig. 8. It was worth noting that the ductility of dual phase ADI is superior to that of conventional ADI, indicating that austempering from the intercritical interval is very effective for improving the ductility of ADI. PF constituent existing in ADI would stabilize austenite against martensite formation by absorbing strain produced by any martensite transformation in RA constituent during deformation [28] and thus effectively enhance the ductility and

mechanical stability of austenite. It should be considered that impact toughness increases at first and then decreases with increasing partially austenitizing temperature, showing the same trend with Chen et al. [19]. Correspondingly, the optimum combination including UTS of 746 MPa, impact toughness of 125 J and E_f of 14% is obtained in D810 composed of 20% PF and 80% AF constituent, in agreement with previous reports [19,23,41]. Fig. 8 also shows Vickers hardness of dual phase ADI as a function of partially austenitizing temperature. The hardness value decreases with decreasing the temperature due to the presence of higher fraction of PF constituent.

Fig. 9 presents fracture surfaces of ADIs. Two distinct regions of different brightness are visible in the surface with the naked eye. It can be seen that higher fraction of AF constituent reduces the dark area while expanding the light area. At a high magnification, micrographs taken from the dark region show an irregular topography with dimples, mainly ascribed to nucleation, growth and coalescence of graphite cavities. Furthermore, the presence of higher amount of AF constituent in matrix structure leads to a decrease in the deformation of nodular cavities. On the other hand, images belonging to the light area predominantly exhibit flat fracture surfaces combined with a few deformed nodular cavities. Meanwhile, with the increasing fraction of AF constituent in matrix structure, the density of river patterns in the flat surface rises, indicating an occurrence of larger deformation. In addition, the fracture surface of C900 shows a uniform distribution of dimples combined with some cleavages. It should be considered that ductile iron features an inherent existence of nodular cavities and possible defects located in the last-to-freeze zones during solidification [41]. Therefore, tensile properties would be governed by the stage of microcrack growth and coalescence. Due to the mechanical property difference in multiphase constituents in dual phase ADI, heterogeneous deformation would occur at the microscale, similar to as-cast ductile iron, as evidenced in previous works [43,44]. At the onset of plastic deformation, the retention of PF constituent allowed great growth of nodular cavities, producing dimple patterns mainly in the dark region. Meanwhile, strain-induced transformation of austenite to martensite in the high strength AF constituent, as observed in previous reports [19,45], led to transformation-induced plasticity during plastic

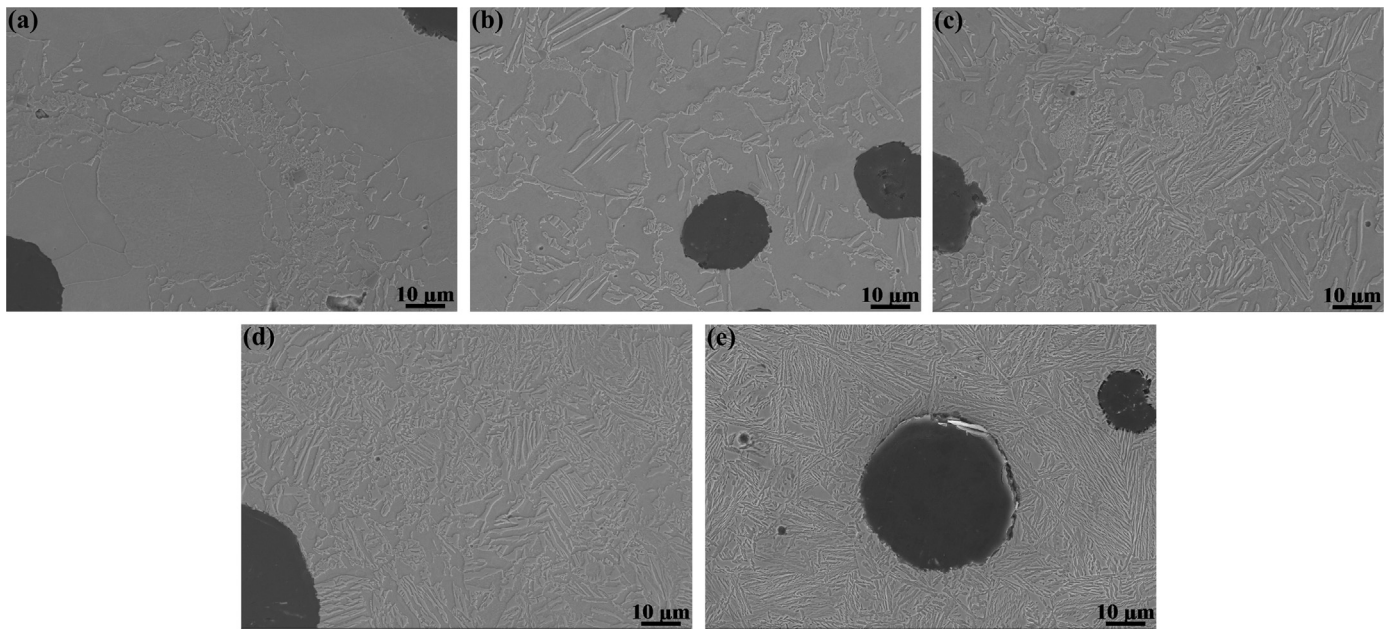


Fig. 5. Microstructural morphology of ADIs: (a) D770, (b) D790, (c) D810, (d) D830, (e) C900.

Table 2
Microstructural characterizations of ADIs.

Group Symbol	Proeutectoid Ferrite (%)	Ausferrite (%)	Austenite (%)	Bainite Ferrite (%)	C _γ (wt %)
D770	94.5	5.5	0	5.5	
D790	55.5	44.5	5.0	39.5	1.72
D810	20.5	79.5	10.4	69.1	1.72
D830	5.4	94.6	13.9	80.7	1.80
C900	0	100	35.3	64.7	1.88

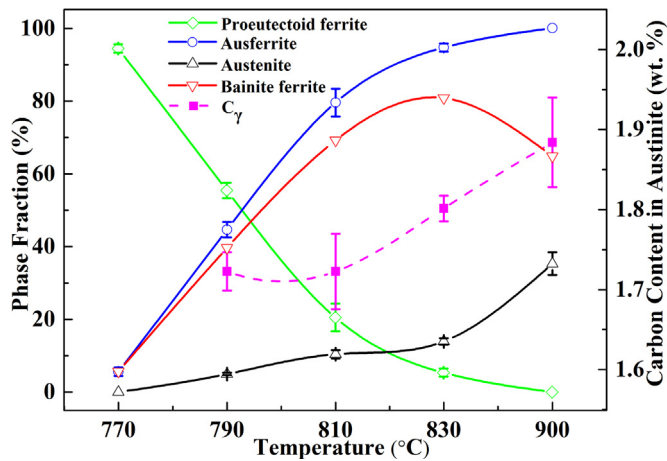


Fig. 6. Microstructural fraction of ADIs as a function of partial austenitizing temperature.

deformation. It is also evident that as the amount of RA constituent increases, the strain-hardening rate increases, as shown in Fig. 9(f). In the final stage of plastic deformation, propagating cracks appeared in the last-to-freeze zones and cleavage fracture took place rapidly, forming the light region, followed by sample rupture.

3.4. Rolling-sliding wear performance

The wear performance of ADI/U75V pairings while cooled by a blast

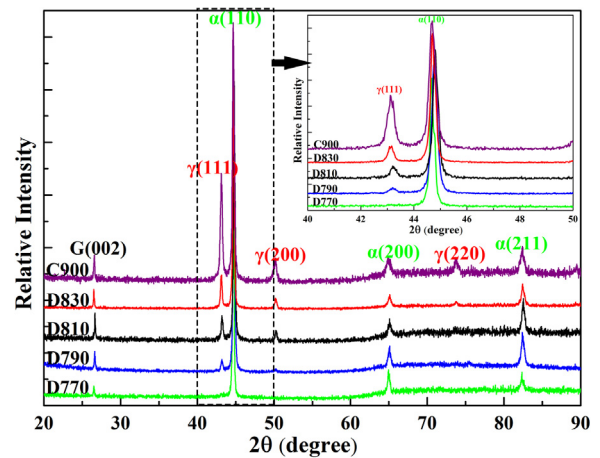


Fig. 7. XRD patterns obtained from ADIs.

Table 3
Mechanical properties of ADIs.

Group Symbol	Ultimate Tensile Strength (MPa)	Yield Strength (MPa)	Elongation (%)	Impact energy (J)	Hardness (HV _{0.05})
D770	520	393	17.9	75	247
D790	655	400	15.8	88	306
D810	746	433	13.8	125	343
D830	871	578	10.0	95	370
C900	1018	694	7.4	105	457
*ER8 [42]	980	600	14		300
*U75V [42]	> 1175		> 9		350

of dry compressed air under a high contact load of 870 N was evaluated. Fig. 10 shows typical evolutions of steady-state friction coefficient with rolling cycles. Despite the same testing condition being used, the friction coefficient differs from each other. For dual phase ADI, the friction coefficient is rather constant during the test, varying between 0.2 and 0.4. It was generally found that the friction coefficient increases with

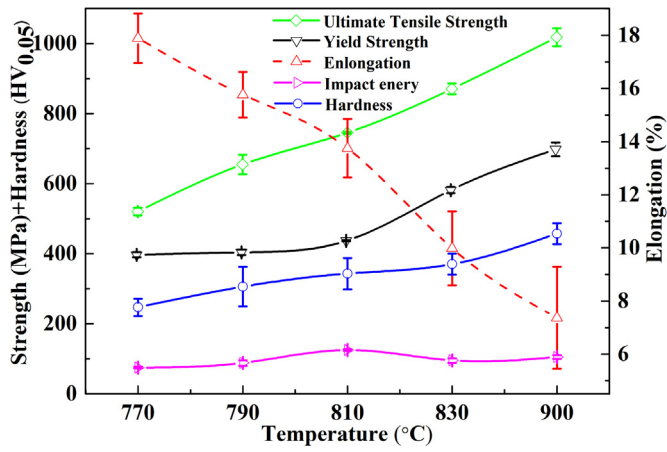


Fig. 8. Mechanical properties as a function of partial austenitizing temperature.

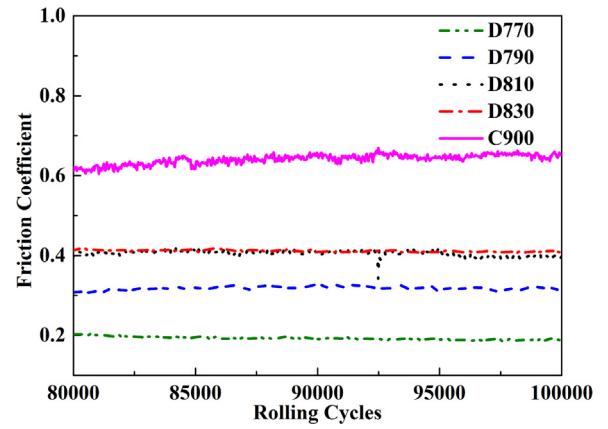


Fig. 10. Evolutions of steady-state friction coefficient with rolling cycles for ADI/rail steel pairings.

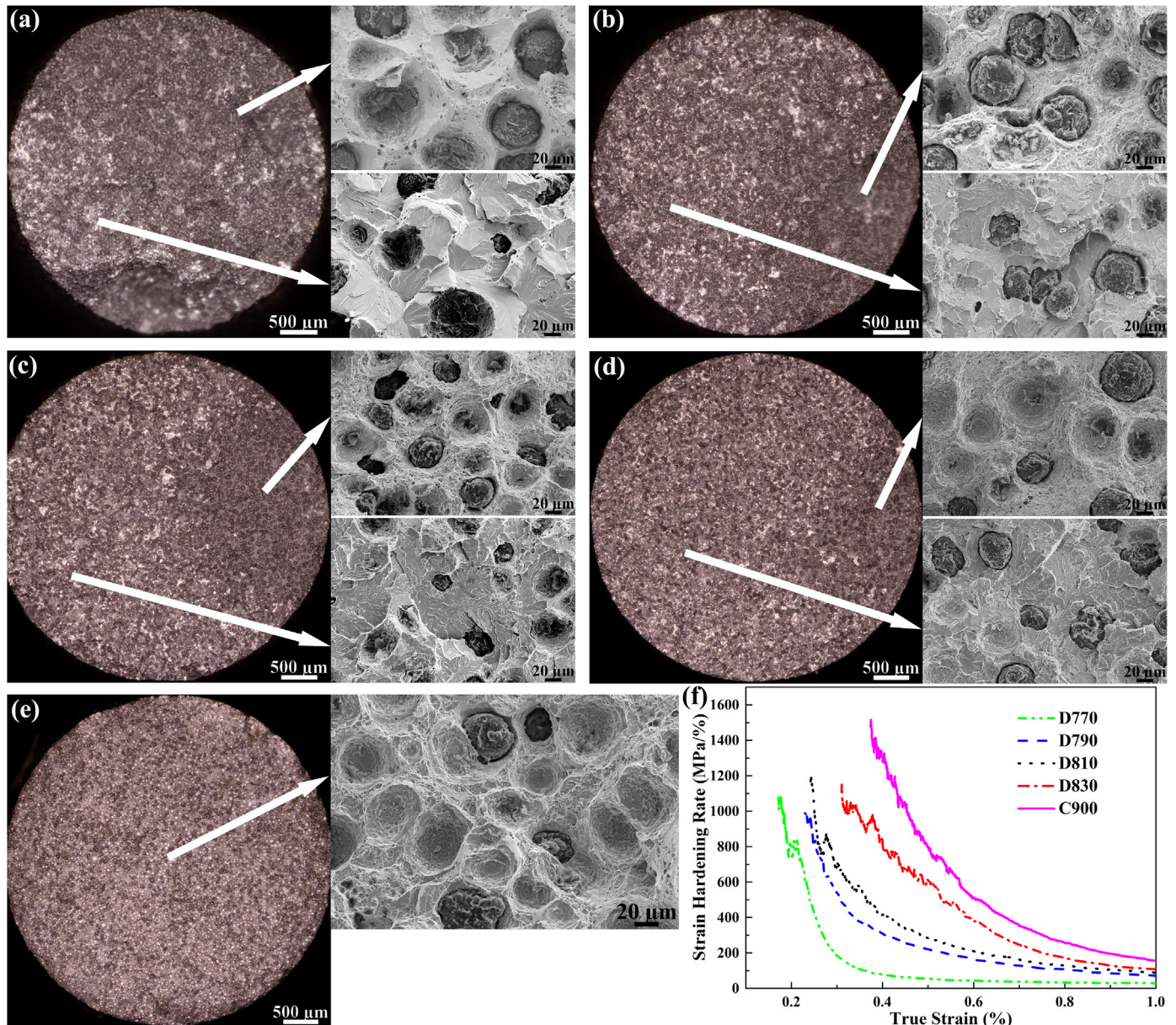


Fig. 9. Fracture surfaces of ADIs: (a) D770, (b) D790, (c) D810, (d) D830, (e) C900, and (f) corresponding strain-hardening rates.

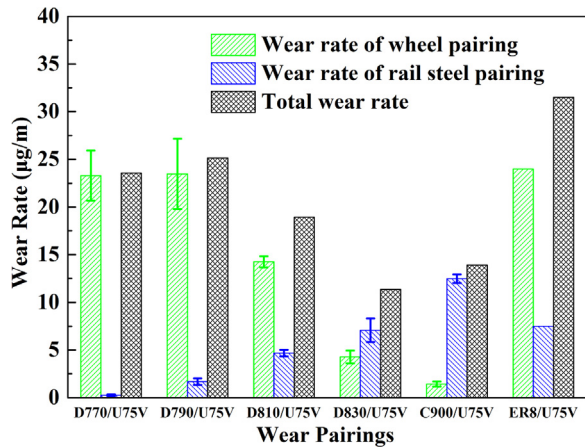


Fig. 11. Average wear rates for ADI/rail steel pairings and conventional wheel/rail steel pairing [27].

increasing matrix hardness, in good accordance with previous investigations [46,47]. Moreover, C900 reveals the highest friction coefficient, as also reported in a previous investigation [3]. Considering that graphite nodules emerging at the contact surface during the test can serve as lubricant [48], dual phase ADI, characterized by the existence of PF constituent, underwent more plastic deformation during the test and resulted in a larger amount of graphite emerging on the contact surface, yielding a lower friction coefficient than conventional ADI. Meanwhile, friction coefficient in this investigation shows a higher value than that in a similar report [49] due to the removal of smeared graphite by the compressed air.

Average wear rates of ADIs matched with U75V are shown in Fig. 11. At low partially austenitizing temperatures, D770 and D790, both having a soft matrix structure, produce the highest wear rate of almost 25 µg/m, indicating the worst wear performance. On the other hand, it was generally found that wear rate decreases with the increase of matrix hardness, even if the increase of friction force, characterized as the friction coefficient under the same contact load. Additionally, the best wear performance is found in C900, which has a wear rate of less

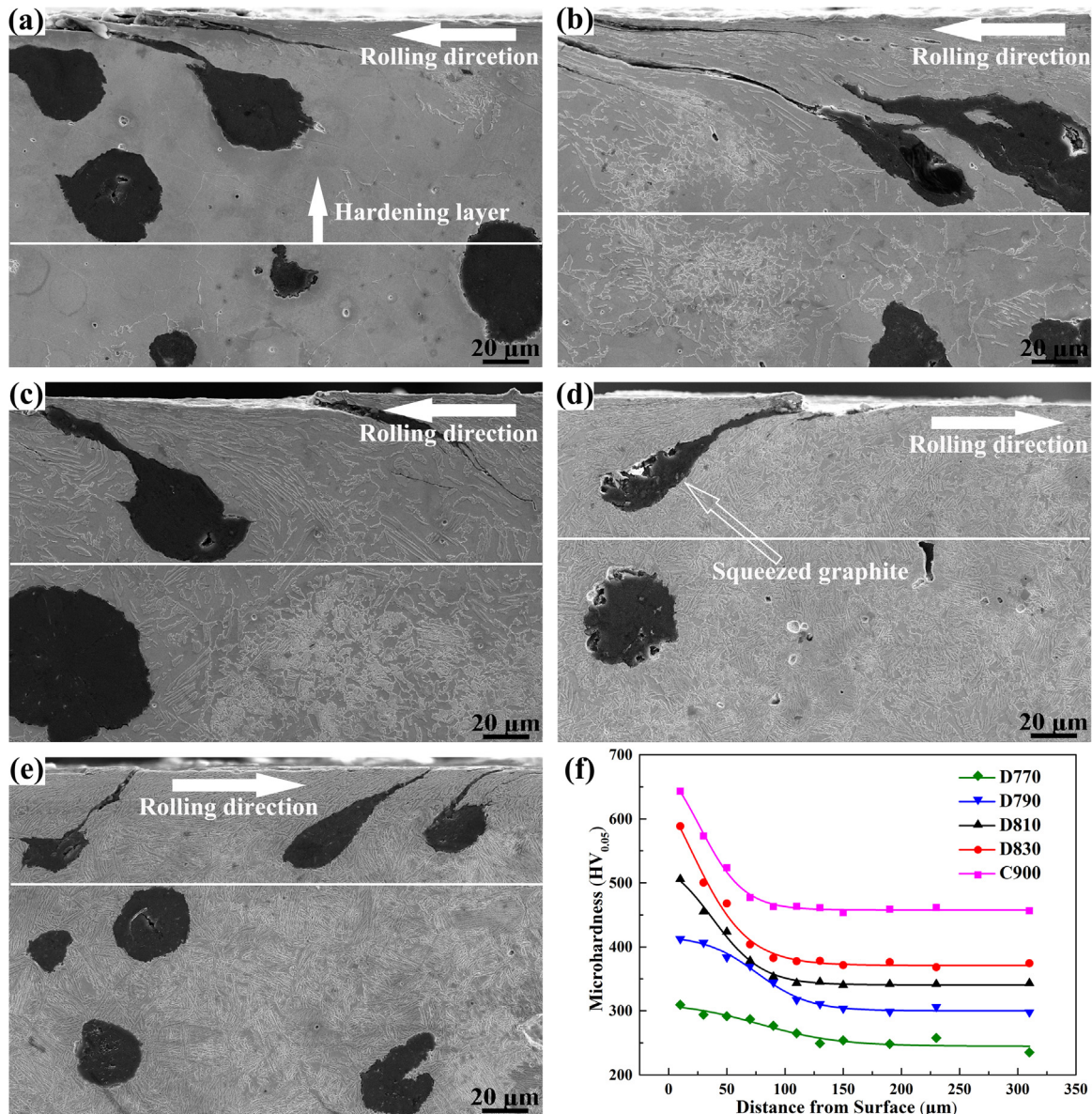


Fig. 12. Cross-section micrographs of worn ADI pairings: (a) D770, (b) D790, (c) D810, (d) D830, (e) C900, and (f) corresponding Vickers hardness distribution of subsurface region.

than 5 $\mu\text{g}/\text{m}$.

Fig. 12 shows cross-section micrographs of worn ADI pairings. As expected, the friction force during the test contributed to large surface shear deformations, forming a ‘hardened layer’, as indicated by white lines. The depth of hardened layer decreases with the increase of matrix hardness. Within the hardened layer, alignment of microstructural features is displayed in the sliding direction and graphite nodules are squeezed to the worn surface during the test, which substantiates the role of graphite nodules as lubricant. Meanwhile, several micro-cracks are found to propagate along the direction of plastic deformation and surround the squeezed graphite nodules owing to weak bonding strength in the matrix-graphite interface [50]. On the other hand, Vickers hardness distribution of subsurface region is plotted in the Fig. 12(f) as a function of distance below the worn surface. As shown, the hardness near worn surface is improved dramatically compared to that of matrix structure and reduces gradually to the initial value for all worn ADI pairings. It should be mentioned that the variation of hardness becomes wider with the decrease of matrix hardness, in good accordance with the cross-section observations.

According to the results above, two major reasons accounts for the formation of hardened layer. Firstly, strain-hardening of matrix structure due to the subsurface deformation induces the hardened layer. XRD patterns of unworn and worn ADI pairings are shown in Fig. 13. The difference in austenite peaks for unworn and worn pairings could be analyzed qualitatively by diffraction patterns. The (111), (200) and (220) planes of FCC reduce to an almost background noise level along with some broadening and enhancement of the (110), (200) and (211) planes of BCC, which indicates the transformation of austenite to martensite. Considering the existence of strain-induced transformation [19,45], secondarily, phase transformation contributes to the formation of hardened layer. In this study, D770 and D790 are characterized by deeper hardened layer and lower hardness value due to the higher fraction of PF constituent, which improves the ductility of the material. Meanwhile, C900 still exhibits the formation of hardened layer despite its higher hardness, which is attributed to the higher fraction of RA constituent. It was therefore concluded that wear behavior could be understood from the manner the hardened layer fragmented and detached.

Fig. 14 presents worn surfaces of all worn ADI pairings. As shown, no brownish oxide particles exists on the worn surface, as confirmed in Fig. 13, which shows no magnetite or hematite peaks in the diffraction patterns. Therefore, oxidation is well prevented by the cooling of compressed air. Meanwhile, spalling layers are distributed on the worn surface, suggesting that ADI pairings underwent wear by delamination due to the subsurface deformation during the test. Additionally, spalling layers exhibits a smaller size with the increase of matrix hardness, indicating mild wear damage. This would explain the variation of

average wear rates.

3.5. Comparison of dual phase ADIs to wheel steel ER8

Taking into account the potential application of dual phase ADI as metro wheel material, it is important to compare wear performance with conventional wheel/rail steel pairings (ER8/U75V) under the same condition, cited from N. Zhang et al. [27] and illustrated in Fig. 11. As shown, D770 and D790 both produce a wear rate of almost 25 $\mu\text{g}/\text{m}$, similar to that of ER8. Furthermore, the others show lower wear rates than ER8. In order to protect rail steel, more attention should be paid to the wear rate of U75V pairing. It rises with increasing matrix hardness of ADI pairing. Meanwhile, worn surfaces of all U75V pairings, as shown in Fig. 15, also exhibit some micropittings and spalling layers indicating that rail steel pairings underwent wear by delamination due to the subsurface deformation and adhesive wear during the test. It was also noted that delamination becomes dominant and severe with increasing the matrix hardness of matched ADI pairing, in good accordance with the variation of average wear rate. In particular, the U75V pairing matched with D830 or C900 exhibits a higher wear rate than that of corresponding ADI pairing, due to lower matrix hardness than that of corresponding ADI pairing. Therefore, this would threaten the service life of rail steel. Accordingly, D810 has relatively favorable wear performance.

Generally, a combination of higher wear resistance and higher fracture toughness should be taken into account in the selection of a proper wheel material [51]. According to the results of mechanical properties, D810 has a combination including UTS of 746 MPa and E_f of 14% and displays the optimal impact toughness. As listed in Table 3, tensile properties of D810 was still lower than that of ER8. Furthermore, it was reported that fracture toughness of dual phase ADI, ranging from 45 to 68 $\text{MPa m}^{1/2}$ [18], is inferior to that of ER8, which shows a value of around 80 $\text{MPa m}^{1/2}$ [52]. However, in view of that metro vehicles are subjected to lower speed and lighter weight during use, the demand of rolling contact strength and fracture toughness for metro vehicles is lower than that for railcars. Besides, dual phase ADI also has some unique advantages of higher damping capacity, lower density and lower manufacturing cost, which are more suitable for metro vehicles. Overall, D810 demonstrates superior wear performance as well as relatively reasonable mechanical properties, suggesting its potential for application in metro wheels.

4. Conclusions

Dual phase ADIs were produced through intercritical austempering. The influence of partially austenitizing temperatures on the mechanical properties and rolling-sliding wear performance of dual phase ADI were investigated. The major conclusions derived from this investigation are:

1. Partial austenitization within the intercritical interval has a profound influence on the amount and morphology of microstructure in dual phase ADI.
2. Dual phase ADI can offer a wide range of mechanical properties depending on its matrix structure. A steady increase is noticed in the UTS and YS with increasing partially austenitizing temperature, while the opposite behavior is observed in the E_f yielding lower values. The optimum combination including UTS of 746 MPa, impact toughness of 125 J and E_f of 14% is obtained in the matrix structure composed of 20% PF and 80% AF constituent. It was also noted that high fraction of AF constituent reduces the dark area, characterized as the irregular topography by dimples, while expanding the light area, which exhibits flat fracture surfaces combined with a few deformed nodular cavities.
3. Wear behavior could be understood from the manner the hardened layer fragmented and detached. The main wear mechanism under the air cooling condition is delamination due to the subsurface

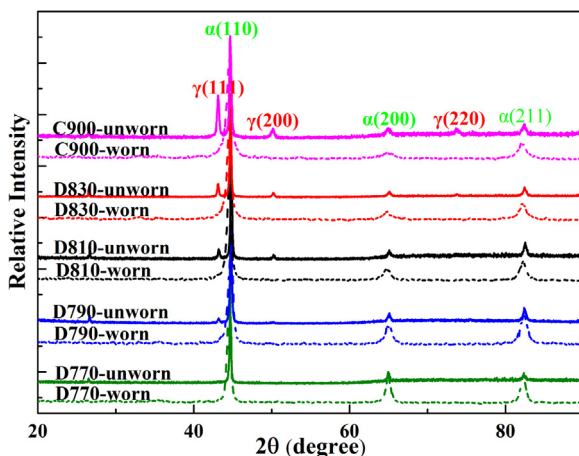


Fig. 13. XRD patterns of unworn and worn ADI pairings.

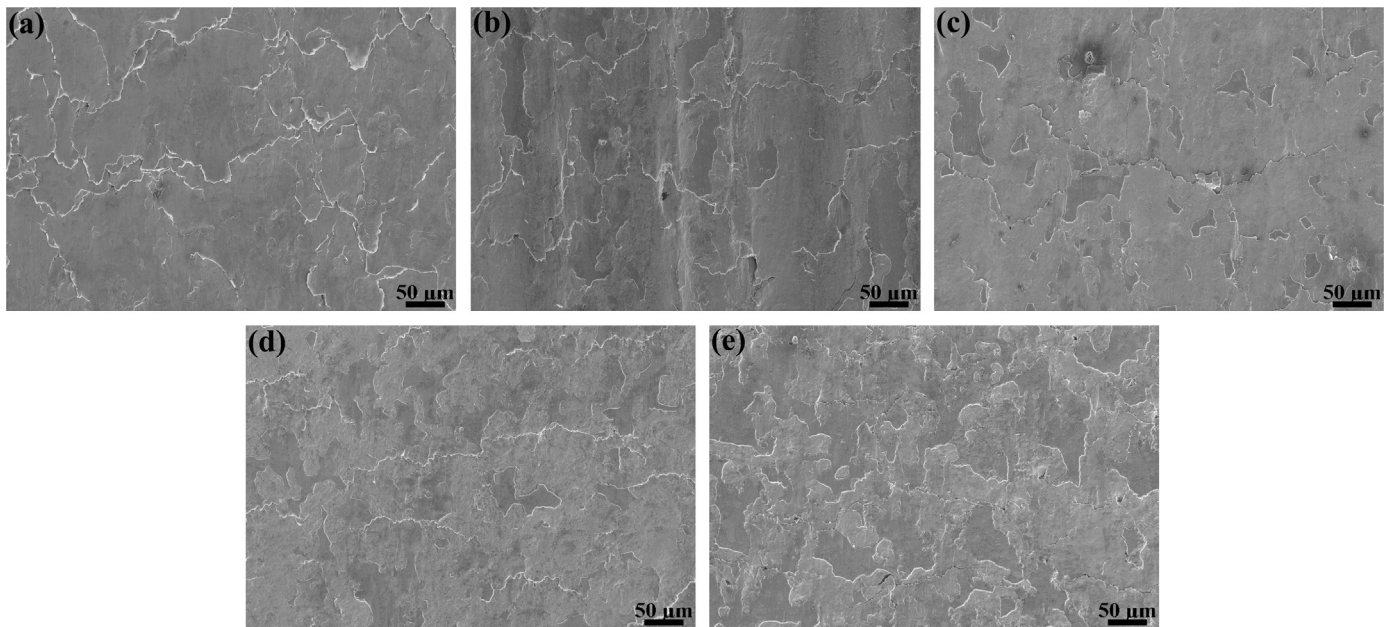


Fig. 14. Worn surfaces of all worn ADI pairings: (a) D770, (b) D790, (c) D810, (d) D830, (e) C900.

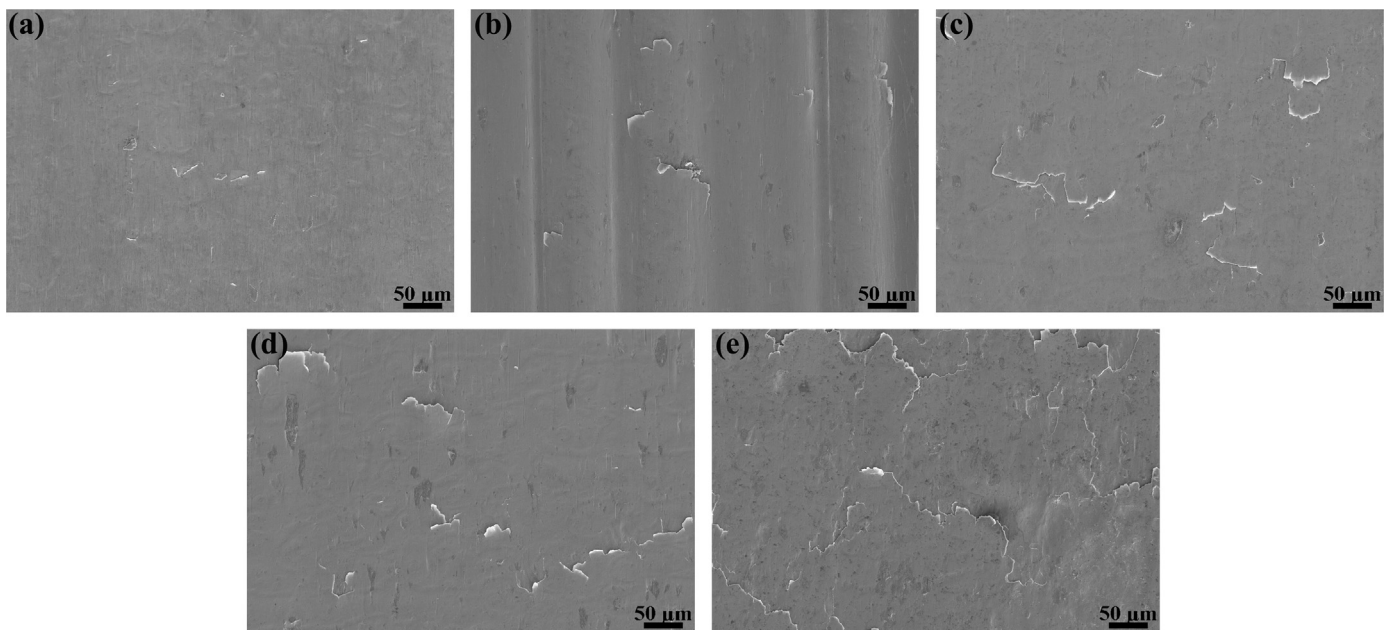


Fig. 15. Worn surfaces of all worn U75V pairings: (a) D770, (b) D790, (c) D810, (d) D830, (e) C900.

deformation. The friction coefficient increases with increasing matrix hardness, varying between 0.2 and 0.4. It was generally found that wear rate decreases as matrix hardness increases.

4. D810 demonstrates superior wear performance as well as relatively reasonable mechanical properties, suggesting its potential for application in metro wheels.

References

- [1] J. Zhang, N. Zhang, M. Zhang, L. Lu, D. Zeng, Q. Song, Microstructure and mechanical properties of austempered ductile iron with different strength grades, *Mater. Lett.* 119 (2014) 47–50.
- [2] A. Basso, R. Martinez, J. Sikora, Influence of section size on dual phase ADI microstructure and properties: comparison with fully ferritic and fully ausferritic matrices, *Mater. Sci. Technol.* 25 (2009) 1271–1278.
- [3] A. Bedolla-Jacuinde, F.V. Guerra, M. Rainforth, I. Mejía, C. Maldonado, Sliding wear behavior of austempered ductile iron microalloyed with boron, *Wear* 330–331 (2015) 23–31.
- [4] S. Solic, M. Godec, Z. Schauperl, C. Donik, Improvement in abrasion wear resistance and microstructural changes with deep cryogenic treatment of austempered ductile cast iron (ADI), *Metall. Mater. Trans. A* 47A (2016) 5058–5070.
- [5] J. Cui, L. Chen, Microstructure and abrasive wear resistance of an alloyed ductile iron subjected to deep cryogenic and austempering treatments, *J. Mater. Sci. Technol.* (2017) 1549–1554.
- [6] C.H. Hsu, K.T. Lin, A study on microstructure and toughness of copper alloyed and austempered ductile irons, *Mater. Sci. Eng. A* 528 (2011) 5706–5712.
- [7] A. Basso, R. Martinez, A.P. Cisilino, J. Sikora, Experimental and numerical assessment of fracture toughness of dual-phase austempered ductile iron, *Fatigue Fract. Eng. Mater. Struct.* 33 (2010) 1–11.
- [8] M.D. Echeverria, O.J. Moncada, J.A. Sikora, Influence of the dimensional change, and its dispersion, on the fabrication size tolerances of austempered ductile iron (ADI) parts: comparison with SAE 4140 steel, *ISIJ Int.* 41 (2001) 25–30.
- [9] A. Sinlah, D. Handayani, R.C. Voigt, K. Hayrynen, R. M'Saoubi, C. Saldana, Effects of microstructure and strength on wear performance in rough milling of austempered ductile iron, *Int. J. Cast. Met. Res.* 29 (2016) 61–66.
- [10] S.F. Liu, Y. Chen, X. Chen, H.M. Miao, Microstructures and mechanical properties of helical bevel gears made by Mn-Cu alloyed austempered ductile iron, *J. Iron Steel*

- Res. Int. 19 (2012) 36–42.
- [11] R. Martins, J. Seabra, L. Magalhães, Austempered ductile iron (ADI) gears: power loss, pitting and micropitting, *Wear* 264 (2008) 838–849.
- [12] J.L. Hernández-Rivera, R.E. Campos Cambranis, A. de la Garza, Study of microstructural evolution and mechanical properties exhibited by non alloyed ductile iron during conventional and stepped austempering heat treatment, *Mater. Des.* 32 (2011) 4756–4762.
- [13] F.V. Guerra, A. Bedolla-Jacuinde, I. Mejia, J. Zuno, C. Maldonado, Effects of boron addition and austempering time on microstructure, hardness and tensile properties of ductile irons, *Mater. Sci. Eng. A* 648 (2015) 193–201.
- [14] S. Panneerselvam, C.J. Martis, S.K. Putatunda, J.M. Boileau, An investigation on the stability of austenite in austempered ductile cast iron (ADI), *Mater. Sci. Eng. A* 626 (2015) 237–246.
- [15] S.C. Murcia, M.A. Paniagua, E.A. Ossa, Development of as-cast dual matrix structure (DMS) ductile iron, *Mater. Sci. Eng. A* 566 (2013) 8–15.
- [16] J. Aranzabal, G. Serramoglia, D. Rousiere, Development of a new mixed (ferritic-ausferritic) ductile iron for automotive suspension parts, *Int. J. Cast. Met. Res.* 16 (2002) 185–190.
- [17] C. Verdu, J. Adrien, A. Reynaud, Contributions of dual phase heat treatments to fatigue properties of SG cast irons, *Int. J. Cast. Met. Res.* 18 (2005) 346–354.
- [18] A.D. Basso, R.A. Martinez, J.A. Sikora, Influence of austenitising and austempering temperatures on microstructure and properties of dual phase ADI, *Mater. Sci. Technol.* 23 (2007) 1321–1326.
- [19] J.K. Chen, B.T. Chen, J.S. Tsai, Microstructural evolutions and properties of partially austenitizing and austempered ductile irons, *Steel Res. Int.* 87 (2016) 191–198.
- [20] S. Panneerselvam, S.K. Putatunda, R. Gundlach, J. Boileau, Influence of intercritical austempering on the microstructure and mechanical properties of austempered ductile cast iron (ADI), *Mater. Sci. Eng. A* 694 (2017) 72–80.
- [21] A. Basso, J. Sikora, Review on production processes and mechanical properties of dual phase austempered ductile iron, *Int. J. Met.* 6 (2012) 7–14.
- [22] A. Basso, R. Martinez, J. Sikora, Influence of chemical composition and holding time on austenite (γ)-ferrite (α) transformation in ductile iron occurring within the intercritical interval, *J. Alloy. Compd.* 509 (2011) 9884–9889.
- [23] A. Basso, M. Caldera, M. Chapetti, J. Sikora, Mechanical characterization of dual phase austempered ductile iron, *ISIJ Int.* 50 (2010) 302–306.
- [24] J. Tunna, J. Sinclair, J. Perez, A review of wheel wear and rolling contact fatigue, *Proc. Inst. Mech. Eng. F.-J. Rai* 221 (2007) 271–289.
- [25] K. Jokipi, Kymenite in Railway Applications, Conference Group of the ADI-Seminar, Technical University Helsinki, 1991, pp. 1–16.
- [26] S. Dündar, Application of austempered ductile iron to rail wheel sets, *J. Eng. Sci.* 9 (2003) 283–287.
- [27] N. Zhang, J.W. Zhang, L.T. Lu, M.T. Zhang, D.F. Zeng, Q.P. Song, Wear and friction behavior of austempered ductile iron as railway wheel material, *Mater. Des.* 89 (2016) 815–822.
- [28] Y. Sahin, M. Erdogan, V. Kilicli, Wear behavior of austempered ductile irons with dual matrix structures, *Mater. Sci. Eng. A* 444 (2007) 31–38.
- [29] V. Gerval, J. Lacaze, Critical temperature range in spheroidal graphite cast irons, *ISIJ Int.* 40 (2000) 386–392.
- [30] R.M. Ghergu, J. Sertucha, Y. Thebault, J. Lacaze, Critical temperature range in standard and Ni-bearing spheroidal graphite cast irons, *ISIJ Int.* 52 (2012) 2036–2041.
- [31] B.D. Cullity, *Elements of X-Ray Diffraction*, Addison-Wesley, Reading, MA, 1974.
- [32] K.B. Rundman, R.C. Klung, X-ray and metallographic study of an austempered ductile cast iron, *Am. Foundry Soc. Trans.* 90 (1982) 499–508.
- [33] F.R. Wilson, R.A. Harding, Effect of carbon on the lattice parameter of austenite, *BCIRA J.* 32 (1984) 318–326.
- [34] ASTM E8/ESM, Standard Test Methods for Tension Testing of Metallic Materials, 3 Annual Book of ASTM Standards, 2012, pp. 77–97.
- [35] G.T. 12444.1, *Metallic materials-wear tests MM mode wear test*, Standardization Administration of the People's Republic of China, 1990.
- [36] K.L. Johnson, *Contact Mechanics*, Cambridge University Press, UK, 1985.
- [37] D.O. Fernandino, J.M. Massone, R.E. Boeri, Characterization of the austemperability of partially austenitized ductile iron, *J. Mater. Process. Technol.* 213 (2013) 1801–1809.
- [38] L. Meier, M. Hofmann, P. Saal, W. Volk, H. Hoffmann, In-situ measurement of phase transformation kinetics in austempered ductile iron, *Mater. Charact.* 85 (2013) 124–133.
- [39] P. Saal, L. Meier, X.H. Li, M. Hofmann, M. Hoelzel, J.N. Wagner, W. Volk, In situ study of the influence of nickel on the phase transformation kinetics in austempered ductile iron, *Metall. Mater. Trans. A* 47A (2016) 661–671.
- [40] R.C. Viogt, *Secondary Graphitization in Quenched and Tempered Ductile Cast Iron (Dissertation)*, Madison, 1981.
- [41] A. Basso, J. Sikora, R. Martinez, Analysis of mechanical properties and its associated fracture surfaces in dual-phase austempered ductile iron, *Fatigue Fract. Eng. Mater. Struct.* 36 (2013) 650–659.
- [42] M. Faccoli, C. Petrogalli, M. Lancini, A. Ghidini, A. Mazzu, Effect of desert sand on wear and rolling contact fatigue behavior of various railway wheel steels, *Wear* 396 (2018) 146–161.
- [43] R.A. Martínez, Fracture surfaces and the associated failure mechanisms in ductile iron with different matrices and load bearing, *Eng. Fract. Mech.* 77 (2010) 2749–2762.
- [44] K.A. Kasvayee, E. Ghassemali, K. Salomonsson, S. Sujakhu, S. Castagne, A.E.W. Jarfors, Strain localization and crack formation effects on stress-strain response of ductile iron, *Mater. Sci. Eng. A* 702 (2017) 265–271.
- [45] J.L. Garin, R.L. Mannheim, Strain-induced martensite in ADI alloys, *J. Mater. Process. Technol.* 143–144 (2003) 347–351.
- [46] J. Zhang, N. Zhang, M. Zhang, D. Zeng, Q. Song, L. Lu, Rolling-sliding wear of austempered ductile iron with different strength grades, *Wear* 318 (2014) 62–67.
- [47] D. Zeng, L. Lu, N. Zhang, Y. Zhang, J. Zhang, Investigation on the scuffing resistance of ductile cast iron as affected by fine particle bombardment to produce surface hardened layer and micro-dimpled surface, *Wear* 378 (2017) 174–182.
- [48] V. Fontanari, M. Benedetti, C. Girardi, L. Giordanino, Investigation of the lubricated wear behavior of ductile cast iron and quenched and tempered alloy steel for possible use in worm gearing, *Wear* 350–351 (2016) 68–73.
- [49] G. Straffellini, C. Giuliani, M. Pellizzari, E. Veneri, M. Bronzato, Dry rolling-sliding wear of austempered cast iron, *Wear* 271 (2011) 1602–1608.
- [50] K. Yıldızlı, M.B. Karamış, F. Nair, Erosion mechanisms of nodular and gray cast irons at different impact angles, *Wear* 261 (2006) 622–633.
- [51] U.P. Singh, A.M. Popli, D.K. Jain, B. Roy, S. Jha, Influence of microalloying on mechanical and metallurgical properties of wear resistant coach and wagon wheel steel, *J. Mater. Eng. Perform.* 12 (2003) 573–580.
- [52] X.C. Ren, J. Qi, J.Y. Gao, L. Wen, B. Jiang, G. Chen, H. Zhao, Effects of heating rate on microstructure and fracture toughness of railway wheel steel, *Metall. Mater. Trans. A* 47A (2016) 739–747.